

A Compliant Biomimetic Artificial Finger for Anthropomorphic Robotic Hands via 3D Rapid Prototyping

Zhe Xu, Vikash Kumar, Evangelos Theodorou, Yoky Matsuoka and Emanuel Todorov

Abstract—This paper presents an anthropomorphic robotic finger that is composed of three biomimetic joints whose biomechanics and dynamic properties are close to their human counterparts. By using five pneumatic cylinders, the robotic finger is actuated through a series of simplified antagonistic tendons whose insertion points and moment arms at each joint are inherited from the anatomy of the human finger. The dynamics of the artificial finger is investigated under PID control for the tasks of set point stabilization and disturbance rejection, set point tracking and trajectory tracking. An air dynamic model is empirically derived for controlling the pneumatic system. The kinematic model of the artificial finger system is constructed with help of MuJoCo - a physics engine custom-developed - to simulate the interaction between the finger's joints and tendons. Experimental data of the tendon excursions are used to validate the efficacy of the simulation model.

Index Terms—Biomimetics, compliant joint, anthropomorphic robotic hands, anatomically correct, simulation model.

I. INTRODUCTION

ANTHROPOMORPHIC robotic hands are attracting growing interest of researchers because of their inherent similarity with the human hand that can potentially bring beneficial impact to many aspects of people's lives. Areas such as space exploration, personal assistance, hand prosthetics, and even industrial automation can all be better served with a highly biomimetic artificial hand. Achieving a robotic hand with biomechanics closely resembling our own will allow natural interaction while enabling a leap in prosthetic design. But significant challenges must first be overcome. These challenges include matching the same degrees of freedom (DOFs) of the human hand, possibly for restoring human-level dexterity, replicating human finger compliance to allow safe operation in unstructured human environments, and also designing the actuation system for mimicking the muscle behavior of the human hand. Other large technical obstacles also exist in terms of tactile sensor implementation, weight and size constraints. This paper focuses on the intrinsic biomechanics required to replicate a human hand.

The challenge of designing a whole robotic hand can be further broken down into individual finger design. The fingers of a human hand possess several salient features that are hard to mimic simultaneously, including (1) the unique shape of

the bones at different joints, which determines the degrees of freedom at the joint; (2) a joint capsule formed by fine ligaments, which set the range of motion for the joint and contribute to formation of the finger compliance; (3) cartilage and synovial fluid, enabling low-friction contact between two articulated surfaces [1]; and (4) extensors and flexors, which are originated from the bone insertion points and control the posture and movement of the finger. Most of the existing anthropomorphic robotic hands have not incorporated these biological features due to various constraints [2]–[17].

The first three challenges belong to the domain of robotic hand's joint design. In the past, two types of joint designs have been widely adopted in anthropomorphic robotic hand research. The first type uses standard mechanical components such as hinges, gimbals, linkages, or gears and belts [2]–[14]. Several important features have been achieved in these anthropomorphic robotic hands, including high degrees of modularity [7], built-in actuators [7]–[9], [18], low inertia [8], [17], [18], and extra palmar DOFs [4], [6]. While this methodology promises excellent performance in achieving the right number of DOFs and even mimicking kinematic characteristics of the human finger, it involves considerable systems-level complexity and implementation costs. In addition few of these types of hands possess built-in compliance which is necessary for a human hand to explore uncertainties in the unstructured real world. The second type uses a simplified design with passive compliance for adaptability. These types of hands are often under-actuated [15]–[17], [19], with fewer actuators than degrees of freedom, and therefore reduce overall complexity of the robotic hand's mechanisms. Mechanical compliance is perhaps the simplest way to allow for coupling between joints without enforcing the fixed-motion coupling relationship inherent with gears or linkages. The hand/graspers made in this way often have superior robustness properties and are able to withstand large impacts without damage [19]. But there is also a tradeoff between achieving the desired range of motion of the finger and having a compliant finger joint since the elastic component cannot by itself limit the joint's range of motion.

As for the last challenge of mimicking the extensors/flexors of the human hand, cables, gears, and linkages have been widely used to transmit the motion from the actuators to finger joints. However, researchers have typically considered it as a part of the joint/finger design rather than emphasize it as an independent component. There are many salient features of the human hand that can only be revealed through dynamic interaction with the different objects. For instance, in order to

Authors are with the Department of Computer Science & Engineering, University of Washington, WA 98195, USA
e-mail: zhixu@cs.washington.edu, vikash@cs.washington.edu,
etheodor@usc.edu, yokky@cs.washington.edu,
todorov@cs.washington.edu

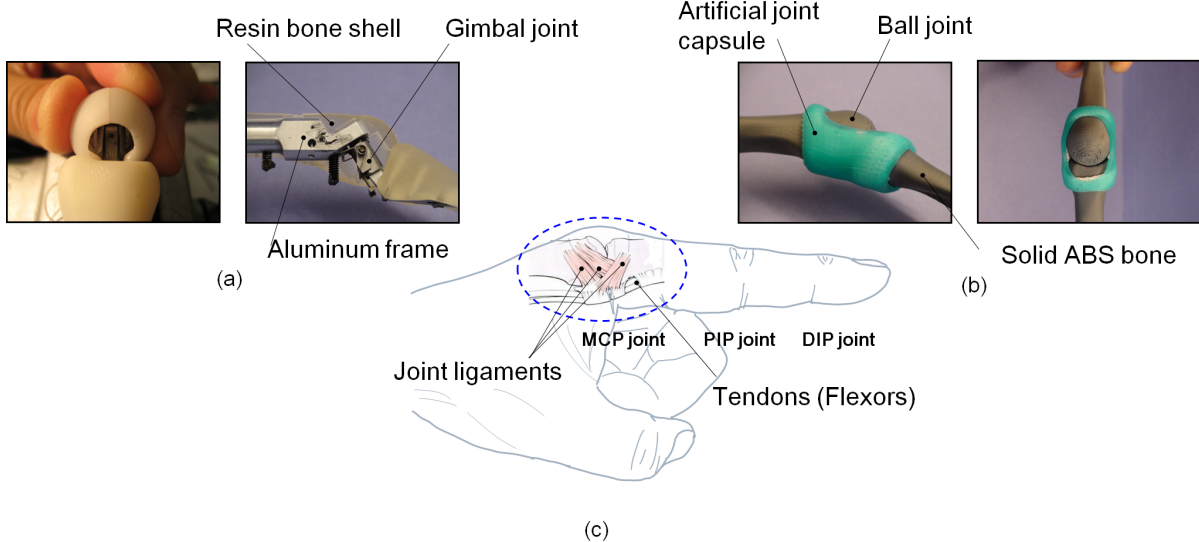


Fig. 1. Comparison of the MCP joint design between the previous and new version of the ACT Hand. (a) Structure of the MCP joint in the previous version of the ACT Hand. (b) Proposed design of the MCP joint described in this paper. (c) Location and anatomy of the MCP joint in the human hand.

understand the variable moment arms, which play a significant role in the movement control of the human finger, researchers rely on constantly modifying the cable routing and improving the design of the extensor hood according to the data collected from physical experiments. Once the complicated, and often expensive anthropomorphic robotic hands are prototyped, researchers are reluctant (when using cables) or won't be able to (when using gears or linkages) modify the transmission pathways without affecting the rest of the components of the robotic hands, resulting in a limited experimental scope.

Although standard design methodology, such as above, can mimic the kinematic behavior of a finger it does little to illuminate the salient features that make the human hand irreplaceable for many dexterous tasks. There is a need for biomimetic artificial fingers, based on accurate physiology, in order to quantitatively identify these characteristics thus providing insight into anthropomorphic robotic hand design.

A compelling alternative to standard mechanical components is to develop mechanisms which directly utilize the unique articulated shapes of human joints, as well as a tendon hood structure to actuate the finger. Following a biologically inspired design also reduces the total number of individual components, resulting in an elegant design.

The robotic finger described in this paper is inspired by the combination of the above approaches and are used as an essential component for the next generation of the Anatomically Correct Testbed (ACT) Hand [20]–[23]. This paper focuses on the design and control of a biomimetic artificial finger composed of three joint capsules whose mechanical structures and dynamic behaviors is similar to that of the human finger [24]. In the following sections the innovative mechanical design methods are detailed, the dynamic behaviors of the artificial MCP joint are analyzed and compared with the human counterpart, the modeling of the pneumatic actuation system is described, then the simulation of the robotic finger is validated through the experimental results.

II. DESIGN OF THE ARTIFICIAL FINGER

The artificial finger discussed in this paper is inspired by the previous version of the ACT Hand. Due to a common ancestor from a cadaver hand both fingers share many biomechanical features such as the length of the bone sections, shape of the joint surfaces, and insertion points of the tendons. However, key differences between the two position our proposed artificial finger into a unique category.

As shown in Figure 1(c), there are three joints in the index finger: namely, the metacarpophalangeal (MCP), proximal interphalangeal (PIP), and distal interphalangeal (DIP). The PIP joint is located at the distal end of the proximal phalangeal bone, and the DIP joint is located at the distal end of the middle phalangeal bone. The MCP joint has two DOFs: one to achieve flexion-extension and another to realize abductionadduction finger motion.

The MCP joint of the ACT Hand's index finger for both the previous and our proposed design are compared with the human counterpart. The anatomical drawing of Figure 1 shows the MCP joint capsule with the extensor hood removed. The previous version of the ACT Hand uses a gimbal joint to realize 2-DOF at the MCP joint. The artificial joint uses a solid sphere which is close to that of a human finger to realize the 2-DOF finger motion (with one extra under-actuated DOF from the 3-DOF spherical joint).

As shown in Figure 1(a), the range of motion of the index finger in the previous design of the ACT Hand is prescribed by the shape of the MCP bone shell. The new design uses crocheted joint ligaments to limit the range of motion of the MCP joint with an elastic sleeve to replicate passive biomechanics of the musculo-skeletal structure. Although the kinematics of the MCP joint in the previous version of the ACT hand matches the human hand very well, a complex motor control strategy must be used in order to simulate the passive biomechanics. Shifting the load of simulating passive biomechanics into physical elastic elements at the joints will

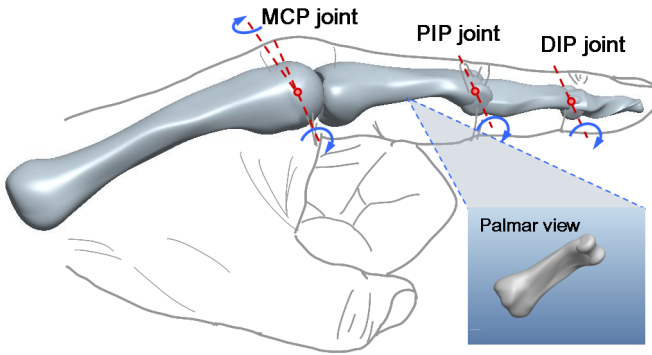


Fig. 2. 3D model of the laser-scanned human index finger.

allow the ACT hand to reduce its control complexity. This not only saves power but also lowers the chance of saturating the actuators with non task-specific commands.

In the following subsections, each of the components of the artificial finger will be introduced according to its assembly sequence.

A. Modular design of the bone segments

In order to anatomically match the size and shape of the human finger bones, we used the index finger from a Stratasys Corporation's laser-scan model of human left hand bones supplied in STL format, imported the tesselate facets into Pro/Engineer, and created solid models for each bone by fitting new surfaces to the scanned geometry [21] (As shown in Figure 2). Detailed parameters of the robotic finger are listed in Table I and II.

TABLE I
PHYSICAL PARAMETERS OF THE ARTIFICIAL FINGER SKELETON

Phalange	Length (mm)	Weight (g)
MCP to PIP	53.4	5.5
PIP to DIP	32.0	2.0
Distal phalange	23.7	1.2

TABLE II
APPROXIMATE JOINT MOTION LIMITS OF THE ARTIFICIAL FINGER

Joint	Minimum	Maximum
MCP	30° extension	90° flexion
	35° abduction	35° adduction
PIP	0° extension	110° flexion
DIP	0° extension	70° flexion

The adoption of an anatomically correct bone structure would seem to imply a cost intensive and complex manufacturing process. However this cost can be avoided through the innovation of rapid prototyping machines. Each section of the finger joint is 3D printed by the Dimension BST 768 (Stratasys Corp., Eden Prairie, MN). The resolution of the 3D printed parts is 0.025 mm, and it takes only three hours to print all the components of the entire index finger. Additionally the

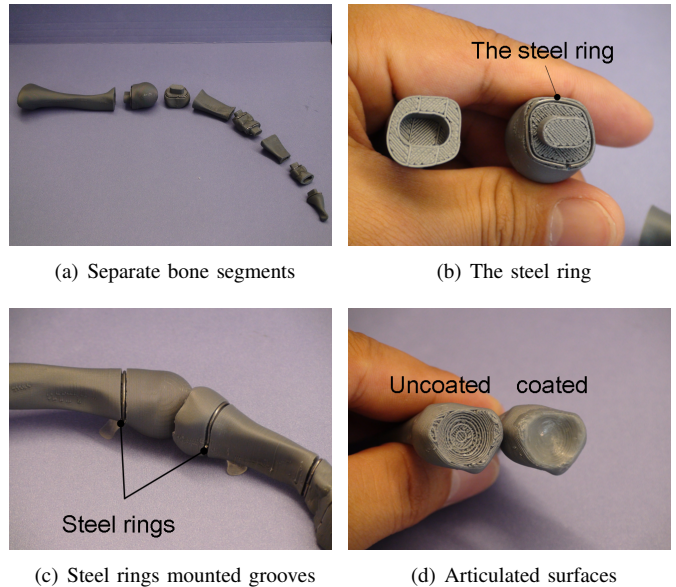


Fig. 3. Components of the index finger bones. (a) Modular design of the index finger. (b) & (c) Steel rings used to anchor the rim of the crocheted finger capsule. (d) Thermoplastic coated articulated surface providing low-friction surface at the finger joint.

strength of the ABS plastic is sufficient to resist the induced stress of the extensor hood.

Each distal section of the finger joint is designed to be detachable from its base as shown in Figure 3 (a). This design serves two functions. The first is for easily mounting a steel ring (0.8mm in diameter) whose shape conforms to the contour of the cross section of the ABS bone. The rim of the crocheted joint capsule is sewn onto this steel ring (Figure 3 (b)) so that the latter forms a continuous attachment zone for the former part along the contour of the cross section near the finger joint. A partially assembled MCP joint section is shown in Figure 3 (c).

The second function of this modular design is to provide a platform for future improvement. For instance, the surface of the ABS parts can be further plated with a 0.003 inch thickness of chrome to provide a better approach to frictionless contact at the finger joint (RePliForm Corp., Baltimore, MD). An instant benefit of this design is also demonstrated in the experiments where different weights of the distal finger are tested for dynamic identification.

In order to mimic the frictionless surface of the articulated cartilage of the human joint a thermoplastic (Shaplock Corp., Sunnyvale, CA) was used to coat the surface of the socket side of the MCP joint as shown in Figure 3 (d). This combination of the joint coupling decreases the friction between the two articulated surfaces. Although, when encountered with the long term tear and wear, commonly engineered materials cannot regenerate like biological tissues, we believe that through low-cost, rapid prototyping technology the modular design can make maintenance of our proposed robotic finger/hand economically viable.

B. Crocheted joint ligaments

In the human hand, the joint capsule is a dense fibrous connective tissue that is attached to the bones via specialized attachment zones and forms a sleeve around the joint. It varies in thickness according to the stresses to which it is subject, and is locally thickened to form capsular ligaments, which may also incorporate tendons (Figure 1). It seals the joint space and provides passive stability by limiting movements through its ligaments [25].

In hand surgery surgeons avoid using mechanically complicated replacements for finger joints. Common prosthetic joints used in hand surgery may include flexible segments made either from titanium alloys, ceramics, or plastics [26] but do not replicate the surface details found on the bone ends. The flexible segments of the prosthetic joint are inserted into holes created inside of neighboring phalanges. The joint is then sealed with the joint capsule. These types of artificial joints have been clinically proven to restore joint function [27]. Without the joint capsule the neighboring phalanges would lose integrity and fall apart, thus it is a critical component of our biologically inspired artificial joint.

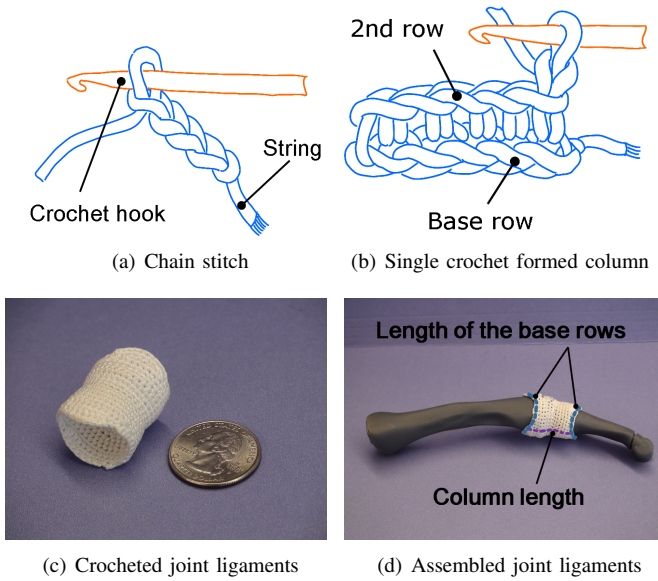


Fig. 4. Crocheted ligaments of the MCP joint. (a) Basic crochet type I – chain stitch. (b) Basic crochet type II – single crochet. (c) Hyperbolic shape of crocheted joint ligaments limits the range of motion of the MCP joint of the index finger. (d) Partially assembled index finger with crocheted ligaments attached.

Our crocheted joint ligaments are fabricated with 0.46mm Spectra® fiber (AlliedSignal, Morristown, NJ). The fiber was chosen because of its strength (200N breaking strength), high stiffness, flexibility, and its ability to slide smoothly over the bones.

Two basic crochet stitches were applied during the fabrication of the artificial ligaments. These are the *chain stitch* and *single crochet* as shown in Figure 4 (a) and (b). A series of chain stitches is called *a row*, the length of the row is determined by the local perimeter of the joint capsule. A single crochet determines the row width, while a double crochet would increase this width. The total width of the chains formed

by single crochet becomes the *column length* of the joint capsule.

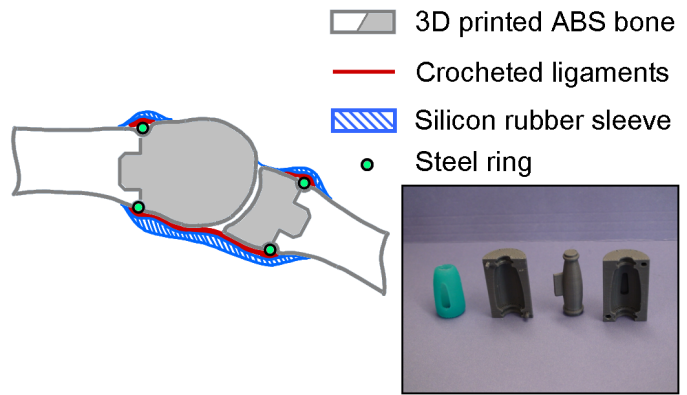


Fig. 5. Cross section of the fully assembled MCP joint. Bottom Right: The silicon rubber sleeve and the molds used for its fabrication.

A sample of crocheted joint ligaments is shown in Fig 4 (c) and (d). This sample illustrates the full hyperbolic shape [28], which covers the area where the extensor hood is typically located. Our design (shown in Figure 1) excludes this dorsal area because the extensor hood is considered as an independent component [29]. The hyperbolic shape of the crocheted ligament is well suited for sealing the joint space, and its column length determines the range of motion of the MCP joint.

Given a fixed distance between the two steel rings the column length then determines the amount of slack in the ligaments with the joint in a neutral position. This slack from the crocheted ligaments constrains the joint's range of motion as it moves. The column length was empirically determined based on the dimension of the joint. The base row for each end of the joint ligaments is formed by a chain whose total length is equal to the perimeter of the steel ring. The local thickness of the joint capsule can also be controlled by varying the number of stitches crocheted on a base row. After fabricating the crocheted joint capsule, it is sewn onto the steel ring which snaps into a groove cut into the bone.

C. Silicon rubber sleeve

Dynamic properties of the finger joints are largely determined by the passive biomechanics of the muscles and tendons which route along the bone surfaces. Rather than mimic the musculo-skeletal properties with an actuator an elastic sleeve can be designed to act on each joint in combination with the crocheted ligaments, recreating the intended dynamics.

The elastic component of the artificial joint is made of silicon rubber (PlatSil® 71 Series RTV, Polytek Development Corp., Easton, PA) with high shear strength. Its shape is cast by a set of 3D printed molds (see Figure 5) which forms a sleeve around the MCP joint providing elastic forces during finger flexion/extension.

To achieve optimal performance and high durability of the silicon rubber, a vacuum chamber was used to remove tiny air bubbles from the silicon mixture before curing. The thickness of the silicon rubber sleeve can be easily modified

by using different molds. This feature provides adjustable stiffness and damping for the artificial joint capsule for our dynamic identification.

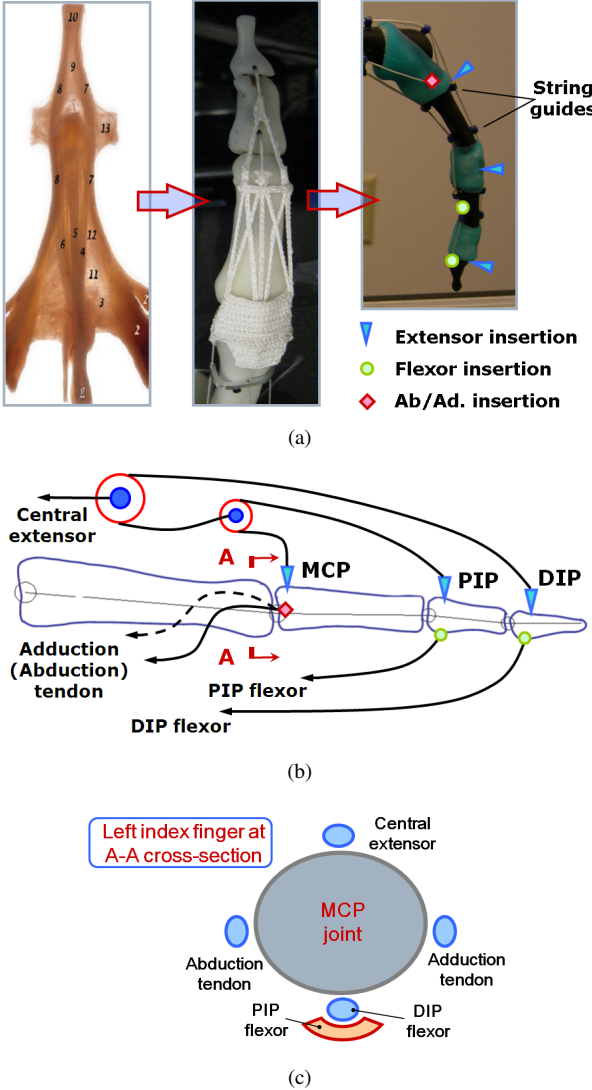


Fig. 6. Comparison of the extensor mechanism between the human hand [30], the ACT Hand and the robotic finger. (a) Design evolution of the tendon hood. (b) Schematic drawing of the pulley system of the artificial finger. (c) Cross-section drawing (A-A) of the tendon structures at the MCP joint for a left index finger (the view is towards the distal aspect of the finger).

D. Tendon hood design and its simplification for the extensor mechanism

Underneath the skin of the human finger over the dorsal side of the finger bone, extension motion of the finger is realized via a complex web structure as shown in the leftmost picture of Figure 6(a). On the palmar side of the finger, antagonistic tendons called flexors are connected from the bone insertion points to the extrinsic muscles located in the forearm to enable the flexion motion.

Previously, a tendon hood for the ACT Hand was designed to mimic the extensor web of the human finger (as shown in the middle picture of 6(a)). The artificial extensor is fabricated by crocheting nylon composite to emulate the geometry and

functionality of the human counterpart as closely as possible. Instead of adopting the same extensor design, in this paper we apply what we have learned from the ACT Hand and keep only the tendons essential for the index finger flexion/extension and abduction/adduction in order to focus on the dynamics and control of our artificial finger.

As shown in the rightmost picture of Figure 6(a), the locations of insertion points and string guides of the artificial finger are all inherited from the human counterpart. The string guides are 3D printed and securely attached to each section of the finger bones allowing for smooth travel of the extensor/flexors. In the case of the human hand, tendons from the three extensor tendons' insertion points are all merged with the extensor hood at the MCP joint, therefore a pulley system is adopted to make sure each individual tendon is constantly in tension (see Figure 6(b)). Our simplified extensor system is designed independently from the joint capsule, thus it reduces the overall complexity of the robotic hand, and makes it cost-effective and flexible enough for future improvement.

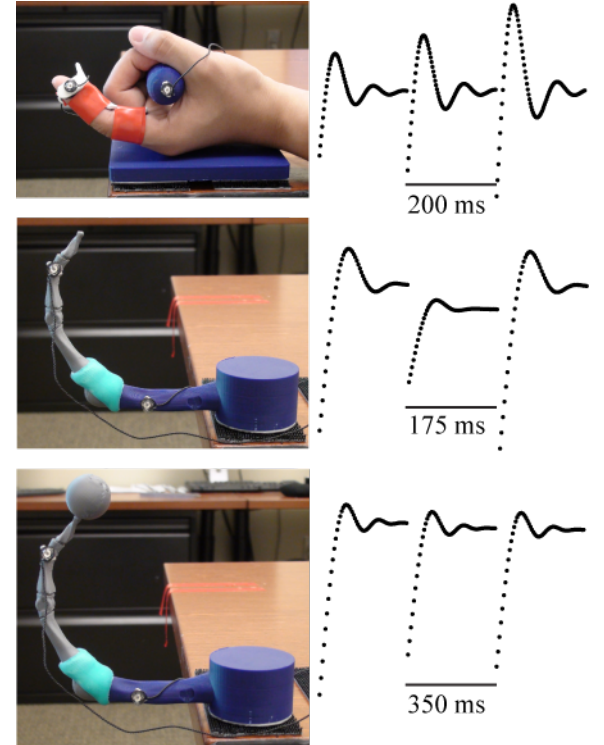


Fig. 7. Left: Experimental setup. Right: typical trials collected from infrared markers for each finger during perturbations. Note that joint angles of the finger postures are 45° at the MCP, 35° at the PIP, and 25° at the DIP.

III. DYNAMICS OF THE ARTIFICIAL JOINT

Together, all of the above components set the stage to enable the artificial finger joint to closely mimic the kinematics and dynamics of the human joint. We quantitatively validate the efficacy of the artificial joint by comparing its dynamic characteristics with that of two human subjects' index fingers by analyzing their impulse response with linear regression. The experimental setup is illustrated in Figure 7. In order to focus on the dynamics of the MCP joint, the base of the hand, DIP,

and PIP joints were all immobilized during the experiments both for the human and robotic finger. The human subjects were instructed to relax and close their eyes, so as to avoid voluntary responses as much as possible.

120 perturbations were applied manually at roughly 1s intervals at the fingertip. In each perturbation the experimenter extended the finger (human or artificial) to a randomly chosen position, and suddenly released it. Infrared markers (PhaseSpace Inc., San Leandro, CA) were attached to the base and distal segments of each finger. The markers' 3D coordinates were measured at 480 Hz using a 7-camera system. The motion capture data was recorded continuously and parsed into individual trials off-line. In some trials a 7.5g mass was also added to the distal segment (8.7g) for investigating the effect of tactile sensors commonly incorporated at the fingertip (as shown in Figure 7 bottom). The rationale was that, if the fingers behaved like mass-spring-damper systems [31], the stopping phase would be particularly revealing with regard to their dynamic properties.

All models were fitted using linear regression (Matlab Statistics toolbox), and all fits reported were significant ($p < 0.05$).

A simple mass-spring-damper model (model M1) was first chosen to fit all datasets:

$$\ddot{\theta} = -k\theta - b\dot{\theta} + a_0 + a_1 \cos(\theta) + a_2 \sin(\theta) \quad (\text{M1})$$

This model was chosen because inertial measurements for the human finger was not viable. Instead of duplicating every detail of the tissues from the human finger, the goal of this artificial joint is to mimic their combined property which can be properly modeled as a spring-damper system. Thus k, b here are the stiffness and damping coefficients divided by the moment of inertia. The term a_0 accounts for the spring reference point, as well as any other potential biases. The trigonometric terms account for gravitational forces.

Model M1 fit the human data quite well (with $R^2 = 0.92$), but provided a rather poor fit for artificial fingers (with average $R^2 = 0.55$), indicating that the latter dynamics are more complex. This problem suggested that the acceleration of the robotic finger may not be a well-defined function of position and velocity, but instead the system may have higher-order dynamics. Plotting the raw data as a 3D scatter plot confirmed our suspicion. Two projections of this 3D plot are shown at the bottom of Figure 8. It is clear that the surface often has two different accelerations for the same point in position-velocity space.

Therefore the data were re-analyzed under the assumption of 3rd-order dynamics. Fig 9 shows the 3D scatter plot of jerk (derivative of acceleration) as a function of velocity and acceleration. It is observed that this function is well-defined (even though there are some positional effects not included in the figure). This prompted us to achieve the final acceleration-based model as follows:

$$\ddot{\theta} = -k\theta - b\dot{\theta} + a_0 + a_1 \cos(\theta) + a_2 \sin(\theta) + c_1\psi + c_2\theta^2 + c_3\dot{\theta}^2 \quad (\text{M2})$$

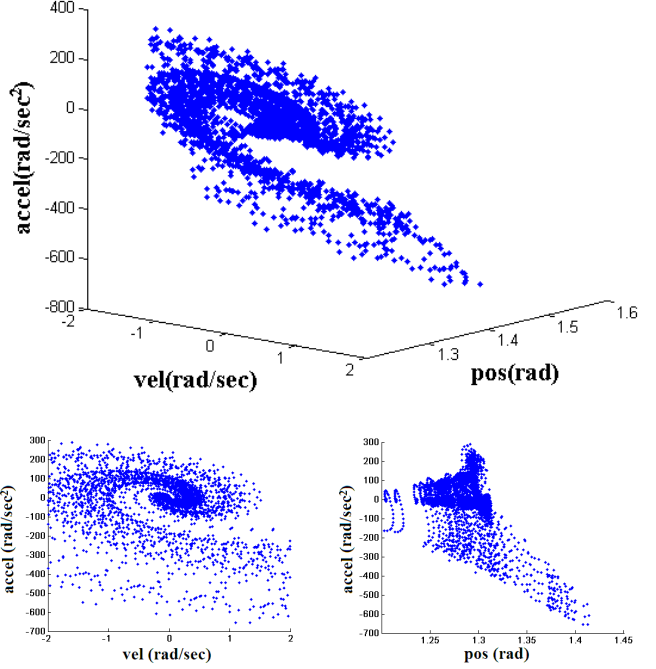


Fig. 8. Top: 3D scatter plot of acceleration vs. velocity and position. Bottom: scatter plots of acceleration vs. position and velocity. All data in this figure are from the artificial finger (unloaded thin).

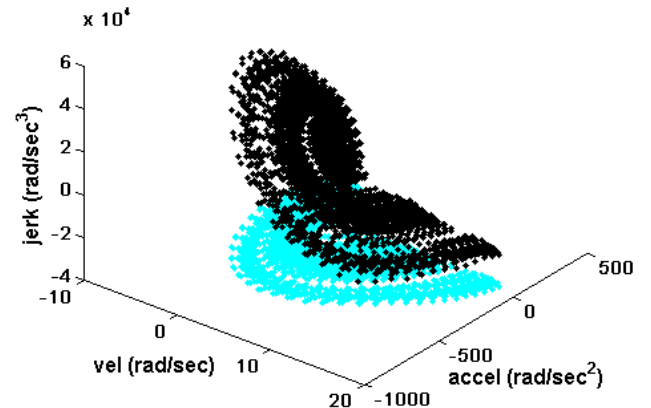
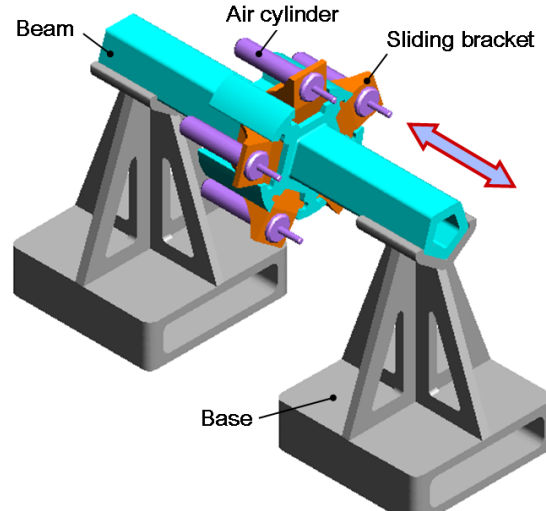


Fig. 9. 3D scatter plot of jerk vs. velocity and acceleration. The light dots are the projection of the data on the bottom plane.

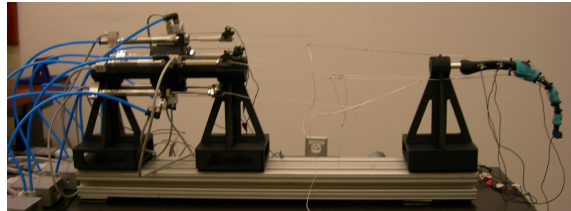
where

$$\psi(t) = \int_0^t \tanh(\dot{\theta}(\tau)) d\tau$$

The quadratic terms $\theta^2, \dot{\theta}^2$ were added so as to allow nonlinear stiffness and damping. The sigmoid (\tanh) term was included as a model of friction. By adopting Model M2, good fits are observed both in the human ($R^2 = 0.97$) and the artificial joint of the index finger ($R^2 = 0.95$). To obtain values for stiffness and damping that can be compared to the values estimated for human finger in [31], a simplified version of model M2 is constructed by removing the quadratic and trigonometric terms. We used an inertia of $0.0006 \text{ kg} \cdot \text{m}^2$ for the unloaded finger (Estimated in Pro/E model) and averaged the results for the thick and thin capsules in the unloaded



(a) 3D model of the actuation system



(b) Experiemntal setup

Fig. 10. The actuation system of the anthropomorphic robotic finger.

condition. The comparison is shown in Table III, the values are quite similar indicating our artificial joint has similar stiffness and damping.

TABLE III
COMPARISON OF STIFFNESS & DAMPING FOR THE HUMAN AND ARTIFICIAL MCP JOINTS

MCP joint of the index finger	Stiffness K (Nm/rad)	Damping B (Nms/rad)
The human joint [31]	0.50 (averaged bewteen -0.2 to 1 radians during MCP flexion)	0.0142 (standard deviation = 0.0023)
The artificial joint	0.534 +/- 0.025 (95% confidence interval)	0.024 +/- 0.0003 ($R^2 = 0.87$)

IV. ACTUATION SYSTEM

The robot finger is actuated using a “Pulling-only pneumatic actuation system” (see Figure 10a). Because of its robustness, smooth dynamics and inherent damping properties, pneumatic actuation seems promising for modeling muscle behaviors. The robotic finger system consists of five double-acting cylinders (Airpel-anti stiction cylinders, model M9D37.5NT2) evenly mounted along the perimeter of a cylindrical beam through five sliding brackets. The sliding brackets are designed to eliminate any potential slack between the tendons and actuators. The pistons of the five cylinders are connected to

the central extensor, abduction and adduction tendons, DIP and PIP flexors, respectively.

The front chamber of each cylinder is connected to a proportional 5/3 pressure valve (Festo, model MPYE-5-M5-010-B). When pressurized the front chamber resembles the muscle contraction and the back chamber is left open to the atmospheric pressure as tendons cannot push the finger (Pulling-only actuation). The valve receives a command voltage from a National Instruments D/A board. This voltage (0-10V) specifies the position of a linear actuator inside the valve, which in turn sets the aperture connecting the front chamber to the compressor (90 PSI above atmospheric pressure). The control command (in V) 5 - 10 pressurizes the systems and 5 - 0 exhausts. The pressure inside the front chamber is measured with a solid-state pressure sensor (SMC, model PSE540-IM5H). The sensor data are sampled at 50 KHz, and averaged in batches of 500 to yield a very clean signal at 100 Hz. The difference between the pressures in the two chambers of each cylinder (denoted D) is proportional to the linear force exerted on the piston. The minimum pressure was hand tuned by raising the pressure in small incremental steps until the cylinder was able to correct for the slacks while finger was moved around. For protection of the finger, each cylinder’s piston contraction is limited by excursion of the tendon it acts upon. Tendon lengths were measured using SICK-cylinder magnetic sensors (sensor resolution is 0.01mm) which linearly scale 32mm over 0-10 volts. SICK sensors were added later, and therefore were not used in the experiments on the kinematic tendon model.

A. Dynamics of the robotic finger system under PID control

This section presents experimental results on the dynamic behavior of the robotic finger system under PID control. In particular, the experiment investigated the combined dynamic behavior of the artificial finger and pneumatic actuation system in three tasks, which are (1) stabilization of the finger at pre-specified positions (set-points) and disturbance rejection; (2) set point change tracking; and (3) trajectory tracking. The PID control policies are constructed over tendon lengths to stabilize the finger at the prespecified set-point. Essentially, the PID control policy of each tendon is only a function of its own tracking error. Thus, control policies do not share tracking error information.

While choosing feasible set-points, each tendon was set to maintain some minimum tension (small pressure in each cylinder thus ensuring that tendons don’t go slack) while the finger was manually moved to a desired configuration. In the human hand, muscles switch from being active and pulling to being passive and stretched. Air cylinders were controlled in the same way in our experiments. Therefore this pulling-only transmission places an interesting constraint to the control system so that a tendon (e.g. PIP extensor) can only correct for the error in one direction (positive errors) and any error in the opposite direction (negative error) is regarded as a positive error for the antagonistic tendon(e.g. PIP flexor) and the artificial finger has to rely on the flexor to correct it.

The robustness of the PID controller and the nonlinearities of the underlying dynamics were investigated, by manually

perturbing the finger (in opposite directions) at different set points. Due to space limitations, this section only provides the results for one set point. The analysis of results focuses on the three tendons, namely, the central extensor, DIP and PIP flexors. Figure 11 summarizes the behavior of the central extensor, DIP, PIP flexors as well as the P, I, D and total control commands for the task of stabilization at horizontal position of the artificial finger. The shaded area (yellow) marks positive errors in a tendon that it can correct by pulling/contracting itself.

Disturbances are applied at $t = 5$ sec and 12 sec. To further investigate the dynamics of the robotic finger system we performed a second experiment in which we changed the set points periodically. In particular, Figure 12 illustrates the dynamic behavior of the main tendons: the central extensor, PIP and DIP in response to periodic changes between three set points during the time horizon of the experiment. Finally in our last experiment we tested the performance of the PID controller for the task of tracking sinusoidal-like trajectories in tendon space. Figure 13 illustrates the results for the central extensor, PIP and DIP tendons.

Our observations regarding the dynamics of the pneumatic index finger are summarized below:

- The stabilization experiment demonstrates that PID control not only stabilizes the artificial finger around a set point but it can also quickly reject disturbances without creating unstable or marginally stable oscillations. It is very characteristic that PID control responds within 2-4 ms of perturbations and can correct for disturbances of magnitude 1.5 cm to the finger tip (2.25mm for central extensor) within 20ms . There is a bias on the central extensor due to weight of the finger that is compensated as the I term of PID accumulates errors over time.
- The response of the pneumatic index finger to disturbances depends a lot on the tuning of the PID gains. Different levels of sensitivity were found to be tendon and posture dependent. Overall, the dynamics of the index finger are more sensitive with respect to the PID gains of the central extensor tendon and the two flexors PIP and DIP and less sensitive to the other two tendons.
- For every stabilization point there is a different set of PID gains (Horizontal Position: $K_p = 0.4$, $K_i = 0.3$, $K_d = 0.005$). Thus, there are no universal PID gains for stabilization and disturbances rejection at different joint space configurations of the finger. The aforementioned observation is an indication of the strong nonlinearities of the underlying dynamics.

The human fingers are actuated through flexors and extensors whose routing and pathway are highly nonlinear, particularly when bones slide over each other at the joints and are constrained by the surrounding soft tissues. The artificial finger biomechanically resembles its human counterpart, therefore the manner in which the tendons interact with the artificial joint capsule change the moment arms as a function of the joint space with respect to different configuration of the artificial finger.

- The performance of the PID control varies in the three tasks of stabilization around one set point, set point

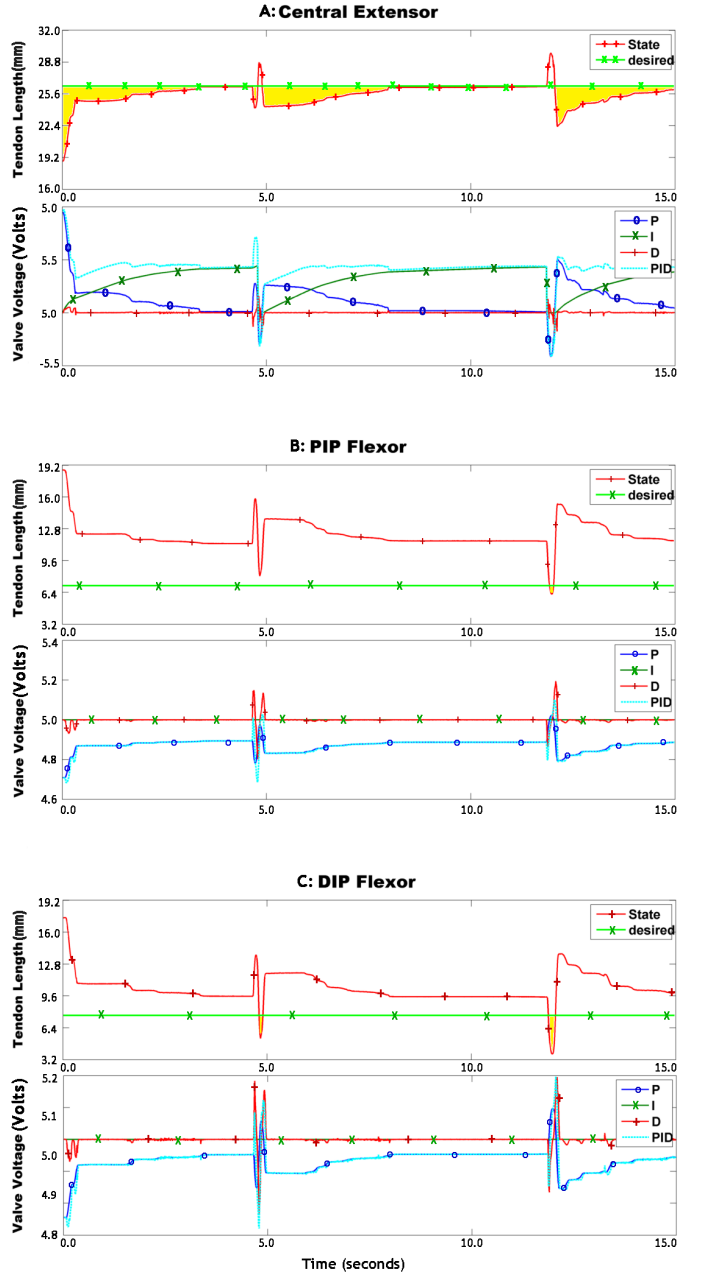


Fig. 11. Desired and actual tendon excursion and PID control commands for the central extensor (A), PIP (B) and DIP (C) tendons for stabilization and disturbance rejection.

tracking and trajectory tracking. Tuning the P, I and D gains for tracking error minimization of a particular tendon does not imply total tracking error minimization. This nonlinear effect arises from the fact that control policies can correct only for positive errors and they have to rely on their opponent(antagonist) for the case of negative errors. Moreover the feedback control of individual tendon does not incorporate tracking errors of other tendons. For such a nonlinear system, a linear controller (PID) can no longer take care of the nonlinearities of the system.

The limitations mentioned above motivate the need for the development of a model based controller that makes informed

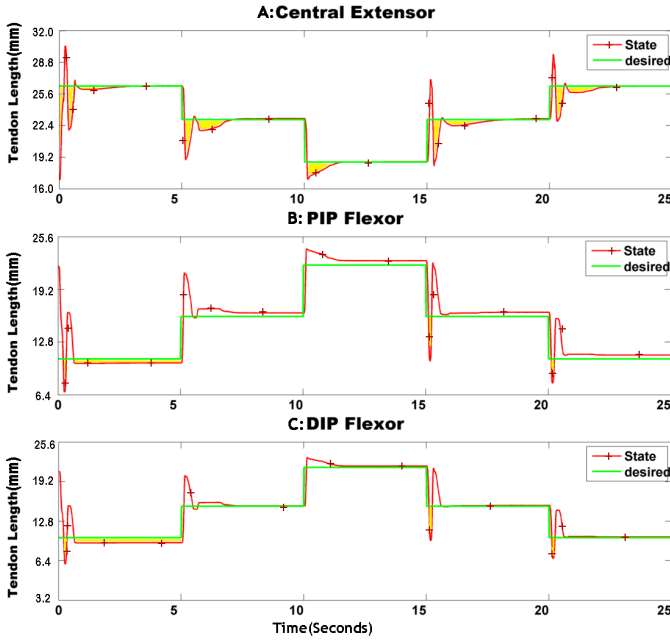


Fig. 12. Desired and actual tendon excursion for central extensor (A), PIP (B) and DIP (C) tendons for the tracking set points task.

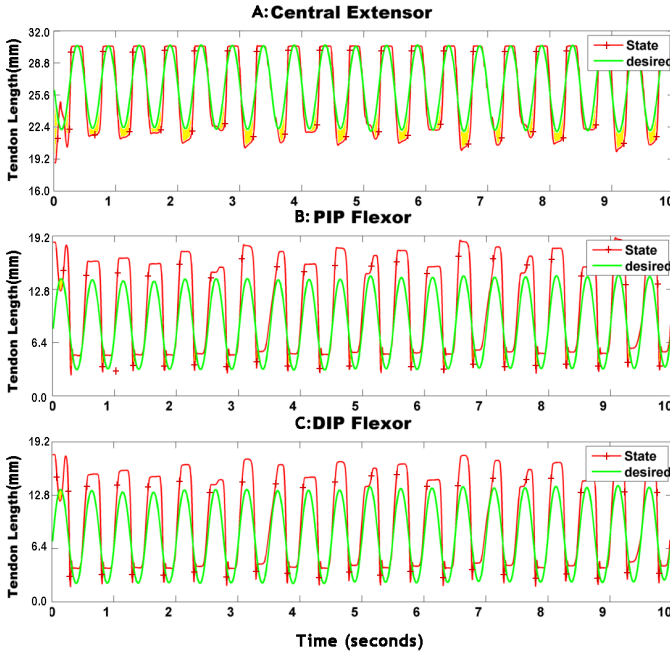


Fig. 13. Desired and actual tendon excursion for central extensor (A), PIP (B) and DIP (C) tendons for the trajectory tracking task.

policy decisions using the entire state space of the tendons while it also takes into account the moment arms at different joint space configurations of the artificial finger.

B. Model based control

Ideally the piston force can be controlled with minimal delay. This is difficult to achieve in pneumatic systems because the air dynamics have non-negligible time constants that depend on multiple factors - compressor pressure, valve throughput and response time, length of the air tubes between

the valve and the cylinder, volume of the chamber, and air temperature. These effects are hard to model accurately, yet for control purposes it is important to have a model that enables the controller to anticipate the resulting delays and compensate for them. To this end, a simple model of how the pressure difference D evolves over time was constructed:

$$dD/dt = A(V) + B(V)D \quad (\text{M3})$$

This is a first-order linear filter, modeling the rate of change of D as a function of the current value of D , and the coefficients A, B which are some to-be-determined functions of the command voltage V . The shape of these functions was measured empirically as follows. A sequence of step voltages (with 2.5 sec duration) was applied, such that D settled into one of its extreme values (V_e), and then was driven towards some intermediate value using an intermediate voltage command(V_i) Figure 14. The piston was fixed in these experiments, so that changes in chamber volume did not affect the results. Figure 15 shows that our simple model is actually quite reasonable. Note that the valves have an internal delay of around 6-7 msec, but after that delay very rapid changes in pressure are observed, with rates on the order of thousands of PSI per second.

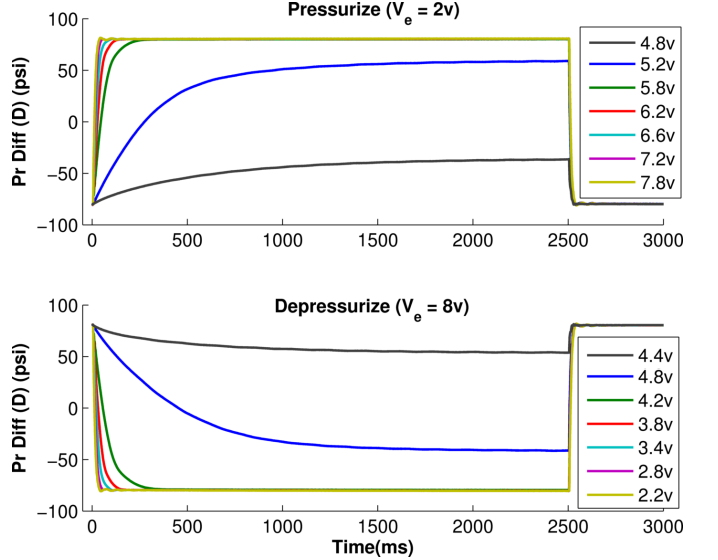


Fig. 14. Pressure difference (D) behavior of pressurization and depressurization at different voltage levels (V_i).

These curves were fitted with exponentials so as to determine the coefficients A, B for every value of V . The resulting coefficients are plotted in Figure 16 as a function of V . This model enables us to implement a high-level controller whose output specifies the desired rate of change in D . We can then invert the functions $A(V)$ and $B(V)$ numerically while keeping D fixed to the currently measured value, and in this way calculate the voltage command V needed to achieve the specified rate of change of D .

C. Kinematic model of the robotic finger system

A kinematic model of the finger skeleton and the tendon paths was constructed. This was done by taking the numeric

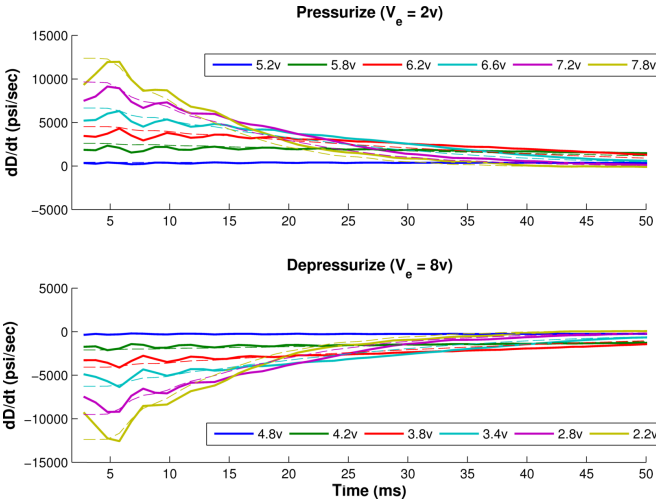


Fig. 15. Pressure difference rate (dD/dt) of pressurization and depressurization at intermediate voltage levels (V_i). Solid lines represent original values and dashed lines represent values predicted by model. Pneumatics incurs a latency of 6-7 msec before reaching its maximum effect.

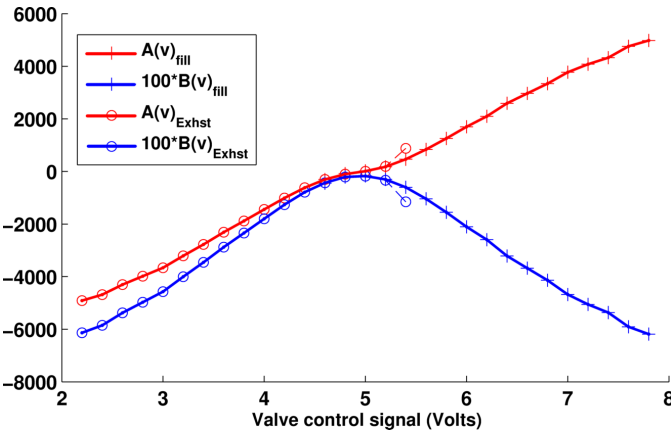
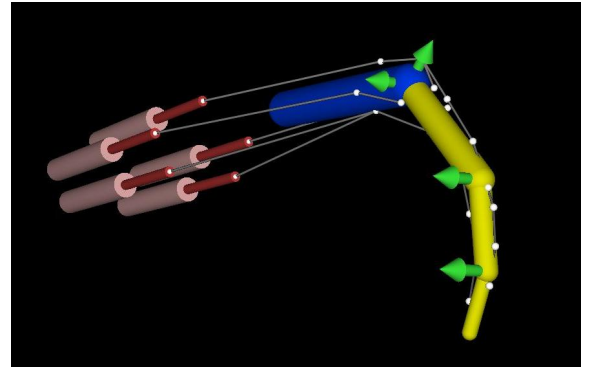


Fig. 16. Coefficients $A(V)$ and $B(V)$ of the valve's air dynamics model.

data from the CAD file used to 3D-print the finger, and importing it in an XML file that was then read by our modeling software. The software – called MuJoCo which stands for Multi-Joint dynamics with Contact – is a full-featured new physics engine, with a number of unique capabilities including simulation of tendon actuation [32]. In this paper the kinematic modeling features of the engine is employed, as well as the built-in OpenGL visualization illustrated in Figure 17.

The skeletal modeling approach is standard: the system configuration is expressed in joint space, and forward kinematics are used at each time step to compute the global positions and orientations of the body segments along with any objects attached to them (such as sites used for tendon routing). Tendon modeling is less common and so our approach will be explained in more detail. The artificial finger is designed so that the tendons can be routed through special attachment points (as opposed to wrapping over curved surfaces). This greatly simplifies the model, because the tendon length is simply the sum of the linear segments connecting the routing points. Of course these lengths change as a function of joint configuration.



(a)



(b)

Fig. 17. Comparison between the MuJoCo based simulation model and the physical prototype. (a) 3D Visualization of the kinematic model of the robotic finger in OpenGL. (b) Proposed biomimetic artificial finger.

Let \mathbf{q} denote the vector of joint angles, and $\mathbf{s}_1(\mathbf{q}), \dots, \mathbf{s}_N(\mathbf{q})$ denote the 3D positions (in global coordinates) of the routing points for a given tendon. These positions are computed using forward kinematics at each time step. Then the tendon length is

$$L(\mathbf{q}) = \sum_{n=1}^{N-1} \left((\mathbf{s}_{n+1}(\mathbf{q}) - \mathbf{s}_n(\mathbf{q}))^T (\mathbf{s}_{n+1}(\mathbf{q}) - \mathbf{s}_n(\mathbf{q})) \right)^{1/2} \quad (M4)$$

The terms being summed are just the Euclidean vector norms $\|\mathbf{s}_{n+1} - \mathbf{s}_n\|$, however they are written explicitly to clarify the derivation of moment arms below.

Moment arms are often defined using geometric intuitions – which work in simple cases but are difficult to implement in general-purpose software that must handle arbitrary spatial arrangements. Instead the more general mathematical definition of moment arm was used in this paper, and is defined as the gradient of the tendon length with respect to the joint angles. Using the chain rule, the vector of moment arms for the tendons is

$$\frac{\partial L(\mathbf{q})}{\partial \mathbf{q}} = \sum_{n=1}^{N-1} \left(\frac{\partial \mathbf{s}_{n+1}(\mathbf{q})}{\partial \mathbf{q}} - \frac{\partial \mathbf{s}_n(\mathbf{q})}{\partial \mathbf{q}} \right)^T \frac{\mathbf{s}_{n+1}(\mathbf{q}) - \mathbf{s}_n(\mathbf{q})}{\|\mathbf{s}_{n+1}(\mathbf{q}) - \mathbf{s}_n(\mathbf{q})\|} \quad (M5)$$

This expression can be evaluated once the site Jacobians $\partial \mathbf{s}/\partial \mathbf{q}$ are known. MuJoCo automatically computes all Jaco-

bians, and so the computation of moment arms involves very little overhead.

The extensor tendon of the artificial finger uses a pulley mechanism, which is modeled as follows. The overall tendon length L is equal to the sum of the individual branches, weighted by coefficients which in this case are $1/2$ for the long path and $1/4$ for the two short paths. Once L is defined, the moment arm vector is computed as above via differentiation.

TABLE IV
MOMENT ARMS THAT THE SIMULATOR COMPUTED IN THE DEFAULT POSTURE (IN MM)

Finger joint	Central extensor	DIP flexor	PIP flexor	Abduction tendon	Adduction tendon
MCP (ab/ad.)	0.00	-0.00	0.00	-8.44	8.86
MCP (fl/ex.)	10.93	-13.47	-13.47	-6.17	-6.06
PIP (fl/ex.)	1.81	-7.99	-7.99	0.00	0.00
DIP (fl/ex.)	1.13	-6.14	0.00	0.00	0.00

Numerical values for the moment arms computed by the model in the resting finger configuration (45° at the MCP, 35° at the PIP, and 25° at the DIP) are shown in Table IV. These values change with finger configuration in a complex way, and are automatically recomputed at each time step. Moment arms are useful for computing the tendon velocities given the joint velocities:

$$\dot{L} = \frac{\partial L(\mathbf{q})}{\partial \mathbf{q}} \dot{\mathbf{q}} \quad (\text{M6})$$

and also for computing the vector of joint torques τ caused by scalar tension f applied to the tendon by the corresponding linear actuator:

$$\tau = \left(\frac{\partial L(\mathbf{q})}{\partial \mathbf{q}} \right)^T f \quad (\text{M7})$$

Note that these are the same mappings as the familiar mappings between joint space and end-effector space, except that the Jacobian $\partial L/\partial \mathbf{q}$ here is computed differently. Another difference of course is that tendons can only pull, so $f \leq 0$.

To validate the kinematic model, the following experiment was conducted. Infrared markers (PhaseSpace, 120 Hz sampling rate) were attached to the fingertip, proximal finger segment, and the moving part of each cylinder. Another 3 markers were attached to the immobile base so as to align the reference frames of the motion capture system and the model. All markers were attached at known positions which we entered into our kinematic model as sites (discrepancy is within 2mm), similar to the sites used to route tendons. The cylinders were pressurized slightly so that they always pulled on the tendons and prevented tendon slack. The artificial finger was manually moved to different poses in its workspace, attempting to span the entire workspace. After each repositioning an interval of a few seconds was used, so as to let everything "settle" and obtain clean position data.

The data analysis began with frame alignment, by subtracting the translational bias between the centers of mass of

the modeled and measured base marker positions, and then performing orthogonal Procrustes analysis to compute the optimal rotation between the motion capture and model frames. The data for the moving markers were then transformed into the model coordinate frame, and were further processed as follows. Our approach implemented a MATLAB script that automatically identified non-overlapping time intervals in which every marker position remained within a ball of radius 2 mm (i.e. all markers were stationary), and averaged the position data for each marker within each time interval. This yielded 460 data points, each consisting of the 3D positions of the 7 mobile markers (5 on the cylinders, 2 on the finger).

The next step was to infer the joint angles of the finger given the positions of the two finger markers. This was done by an automated procedure (which is part of the MuJoCo engine), whereby the residual difference between the observed and predicted marker positions is minimized with respect to the set of joint angles (note that the predicted positions are functions of the joint angles). The minimization is done using a Gauss-Newton method with cubic line-search. Even at the optimal joint angles, there was some residual in the marker positions (around 5 mm on average) which we believe is mostly due to the fact that the finger is somewhat flexible and has additional degrees of freedom (even though their range of motion is very limited). Data points where the residual was larger than 7 mm were excluded from further analysis, leaving us with 400 data points.

Once the joint angles in each pose were inferred, our proposed tendon model was applied to compute the predicted tendon lengths, and the results were compared to the measured positions of the cylinder markers. The comparison is shown in Figure 18 for all five tendons. Overall good fit was observed, especially for the flexors and extensor that have larger excursions. The adduction tendon shows saturation, which might be caused by the position limiter on the cylinder (those limiters were just placed outside the range of the finger motion, but this one ended up inside the range) causing the tendon to go slack in some extreme poses. The abduction tendon is the most noisy, which we believe is due to the fact that it presses on the joint capsule and curves over it. This can be corrected by adjusting the routing points.

V. CONCLUSION AND FUTURE WORK

This paper has described the design and modeling of a biomimetic artificial finger that has the potential to become a close replica of the human finger. The robotic finger system makes use of three main components: a modular design of the 3D printed finger segments, a series of simplified pulley based tendon mechanism, and a model based pneumatic actuation system for mimicking the contraction-only muscle behavior. The series of experiments on stabilization, disturbance rejection and tracking under PID control suggest that our robotic finger system presents a highly non-linear dynamics. The kinematic model of the artificial finger system is constructed with help of MuJoCo - a physics engine custom-developed - to simulate the interaction between the finger's joints and tendons. Experimental data of the tendon excursions are used

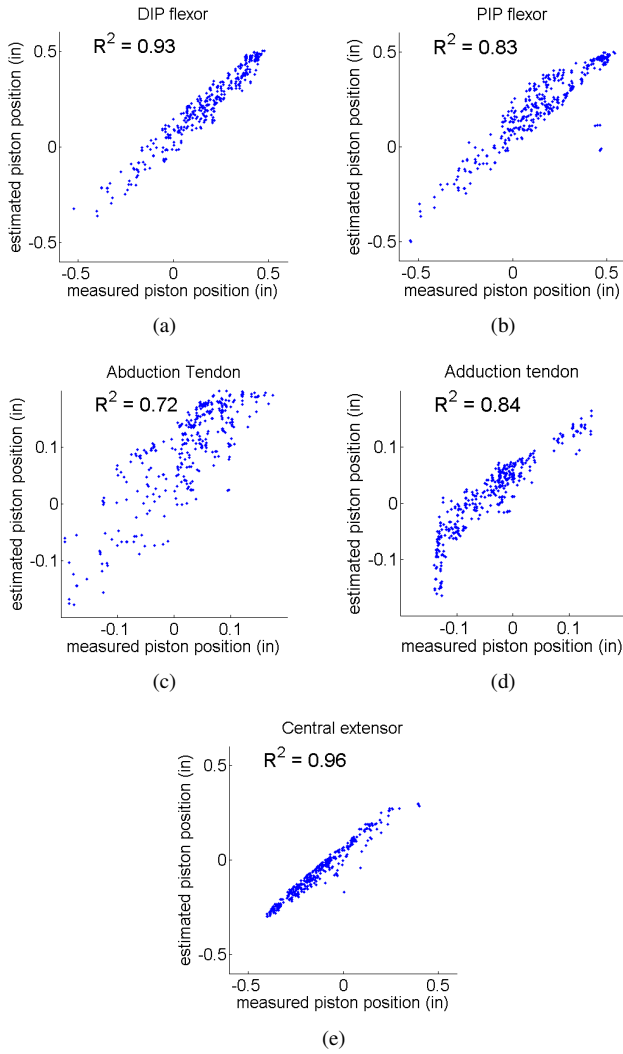


Fig. 18. Comparison of measured and estimated tendon excursion data.

to validate the efficacy of the simulation model. Overall good fits have been observed in the DIP, PIP flexors ($R^2 = 0.93$ and $R^2 = 0.83$) and central extensor ($R^2 = 0.96$) along which large excursions commonly occurred.

Thus far the entire actuation system and models of the kinematics and air dynamics have been built and established for the artificial finger. Our experimental results on stabilization and tracking with PID control motivate our future research towards system identification and model based control. At the system identification level, the next step is to identify the dynamics of the pneumatics and integrate the resulting model with the proposed kinematic model of the skeleton and the tendons. On the control theoretic aspect, additional future work is to use model based techniques with variable sensitivity to model errors and contact discontinuities. These methods span the range of optimal, model predictive control and nonlinear methods such as back-stepping control. We also believe that a deeper understanding of the unique features in human hands will provide greater insight into future designs of anthropomorphic robotic hands.

REFERENCES

- [1] P. W. Brand and M. H. Anne, *Clinical Mechanics of the Hand*. St. Louis: Mosby-Year Book, Inc., 1993.
- [2] G. Bekey, R. R. Tomovic, and I. Zeljkovic, "Control architecture for the belgrade/USC hand," *Dextrous Robot Hands.*, pp. 136–149, 1990.
- [3] S. Jacobsen, E. Iversen, D. Knutti, R. Johnson, and K. Biggers, "Design of the Utah/M.I.T. dexterous hand," vol. 3, pp. 1520–1532, Apr 1986.
- [4] C. Lovchik and M. Diftler, "The Robonaut hand: a dexterous robot hand for space," in *Proceedings of the 1999 IEEE International Conference on Robotics and Automation.*, vol. 2, 1999, pp. 907–912.
- [5] T. Mouri, H. Kawasaki, Y. Keisuke, J. Takai, and S. Ito, "Anthropomorphic robot hand: Gifu hand III," in *Proc. Int. Conf. ICAS*, 2002.
- [6] Shadow Robot Company, "www.shadowrobot.com," 2008.
- [7] J. Butterfass, M. Fischer, M. Grebenstein, S. Haidacher, and G. Hirzinger, "Design and experiences with DLR hand II," vol. 15, 2004, pp. 105–110.
- [8] I. Yamano and T. Maeno, "Five-fingered robot hand using ultrasonic motors and elastic elements," in *Proceedings of the 2005 IEEE International Conference on Robotics and Automation.*, April 2005, pp. 2673–2678.
- [9] J. Ueda, Y. Ishida, M. Kondo, and T. Ogasawara, "Development of the NAIST-Hand with vision-based tactile fingertip sensor," 2005.
- [10] M. C. Carrozza, G. Cappiello, S. Micera, B. B. Edin, L. Beccai, and C. Cipriani, "Design of a cybernetic hand for perception and action," *Biol. Cybern.*, vol. 95, no. 6, pp. 629–644, 2006.
- [11] Touch Bionics Inc., "www.touchbionics.com," 2009.
- [12] DEKA Research and Development Corp., "www.dekareresearch.com," 2008.
- [13] S. Dalley, T. Wiste, T. Withrow, and M. Goldfarb, "Design of a multifunctional anthropomorphic prosthetic hand with extrinsic actuation," *IEEE/ASME Transactions on Mechatronics*, vol. 14, no. 6, pp. 699–706, dec. 2009.
- [14] M. Carrozza, B. Massa, S. Micera, R. Lazzarini, M. Zecca, and P. Dario, "The development of a novel prosthetic hand-ongoing research and preliminary results," *IEEE/ASME Transactions on Mechatronics*, vol. 7, no. 2, pp. 108–114, jun. 2002.
- [15] P. J. Kyberd, C. Light, P. H. Chappell, J. M. Nightingale, D. Whatley, and M. Evans, "The design of anthropomorphic prosthetic hands: A study of the southampton hand," *Robotica*, vol. 19, no. 6, pp. 593–600, 2001.
- [16] M. C. Carrozza, C. Suppo, F. Sebastiani, B. Massa, F. Vecchi, R. Lazzarini, M. R. Cutkosky, and P. Dario, "The spring hand: Development of a self-adaptive prosthesis for restoring natural grasping," *Autonomous Robots*, vol. 16, no. 2, pp. 125–141, 2004.
- [17] F. Lotti, P. Tiezzi, G. Vassura, L. Biagiotti, G. Palli, and C. Melchiorri, "Development of UB Hand 3: Early results," in *Proceedings of the 2005 Five-fingered robot hand using ultrasonic motors IEEE International Conference on Robotics and Automation*, April 2005, pp. 4488–4493.
- [18] H. Kawasaki, T. Komatsu, and K. Uchiyama, "Dexterous anthropomorphic robot hand with distributed tactile sensor: Gifu hand II," *IEEE/ASME Transactions on Mechatronics*, vol. 7, no. 3, pp. 296 – 303, sep. 2002.
- [19] A. Dollar and R. Howe, "A robust compliant grasper via shape deposition manufacturing," *IEEE/ASME Transactions on Mechatronics*, vol. 11, no. 2, pp. 154 –161, april 2006.
- [20] D. Wilkinson, M. Vande Weghe, and Y. Matsuoka, "An extensor mechanism for an anatomical robotic hand," in *Proceedings of the 2003 IEEE International Conference on Robotics and Automation*, 2003.
- [21] M. Vande Weghe, M. Rogers, M. Weissert, and Y. Matsuoka, "The ACT hand: Design of the skeletal structure," in *Proceedings of the 2004 IEEE International Conference on Robotics and Automation*, 2004.
- [22] L. Y. Chang and Y. Matsuoka, "A kinematic thumb model for the ACT hand," in *Proceedings of the 2006 IEEE International Conference on Robotics and Automation*, 2006.
- [23] A. D. Deshpande, Z. Xu, M. J. V. Weghe, B. H. Brown, J. Ko, L. Y. Chang, D. D. Wilkinson, S. M. Bidic, and Y. Matsuoka, "Mechanisms of the Anatomically Correct Testbed Hand," *IEEE/ASME Transactions on Mechatronics*, no. 99, pp. 1–13, 2011.
- [24] Z. Xu, E. Todorov, B. Dellon, and Y. Matsuoka, "Design and analysis of an artificial finger joint for anthropomorphic robotic hands," in *2011 IEEE International Conference on Robotics and Automation (ICRA)*, May 2011, pp. 5096 – 5102.
- [25] J. R. Ralphs and M. Benjamin, "The joint capsule: structure, composition, ageing and disease," *Journal of Anatomy*, vol. 3, pp. 503–509, 1994.

- [26] T. Joyce, "Currently available metacarpophalangeal prostheses: their designs and prospective considerations," *EXPERT REVIEW OF MEDICAL DEVICES*, vol. 1, no. 2, pp. 193–204, NOV 2004.
- [27] D. Beevers and B. Seedhom, "Metacarpophalangeal joint prostheses: A review of the clinical results of past and current designs," *The Journal of Hand Surgery: Journal of the British Society for Surgery of the Hand*, vol. 20, no. 2, pp. 125 – 136, 1995.
- [28] D. Henderson and D. Taimina, "Crocheting the hyperbolic plane," *MATHEMATICAL INTELLIGENCER*, vol. 23, no. 2, pp. 17–28, SPR 2001.
- [29] F. H. Netter, *Atlas of Human Anatomy*, 2nd ed. Teterboro, New Jersey: Icon Learning Systems, 1997.
- [30] J. Clavero, P. Golano, O. Farinas, X. Alomar, J. Monill, and M. Esplugas, "Extensor mechanism of the fingers: MR imaging-anatomic correlation," *RADIOGRAPHICS*, vol. 23, no. 3, pp. 593–611, MAY-JUN 2003.
- [31] D. G. Kamper, T. G. Hornby, and W. Z. Rymer, "Extrinsic flexor muscles generate concurrent flexion of all three finger joints," *Journal of Biomechanics*, vol. 35, no. 12, pp. 1581 – 1589, 2002.
- [32] E. Todorov, T. Erez, and Y. Tassa, "Mujoco: a physics engine for model-based control," *Under Review*.